



RESEARCH ARTICLE

10.1002/2014JB011395

Key Points:

- InSAR and microseismic study following the 2011 eruption at Nabro, Eritrea
- InSAR shows subsidence, best modeled by a Mogi source at 6 km depth
- Seismicity suggests that subsidence is controlled by changes in the magma chamber

Supporting Information:

- Readme
- Figure S1
- Figure S2

Correspondence to:

J. E. Hamlyn,
ee10j2h@leeds.ac.uk

Citation:

Hamlyn, J. E., D. Keir, T. J. Wright, J. W. Neuberg, B. Goitom, J. O. S. Hammond, C. Pagli, C. Oppenheimer, J.-M. Kendall, and R. Grandin (2014), Seismicity and subsidence following the 2011 Nabro eruption, Eritrea: Insights into the plumbing system of an off-rift volcano, *J. Geophys. Res. Solid Earth*, 119, 8267–8282, doi:10.1002/2014JB011395.

Received 19 JUN 2014

Accepted 22 AUG 2014

Accepted article online 2 SEP 2014

Published online 13 NOV 2014

The copyright line for this article was changed on 19 DEC 2014 after original online publication.

This is an open access article under the terms of the Creative Commons Attribution License, which permits use, distribution and reproduction in any medium, provided the original work is properly cited.

Seismicity and subsidence following the 2011 Nabro eruption, Eritrea: Insights into the plumbing system of an off-rift volcano

Joanna E. Hamlyn¹, Derek Keir², Tim J. Wright¹, Jürgen W. Neuberg¹, Berhe Goitom³, James O. S. Hammond⁴, Carolina Pagli⁵, Clive Oppenheimer⁶, J-Michael Kendall³, and Raphaël Grandin⁷

¹COMET, School of Earth and Environment, University of Leeds, Leeds, UK, ²National Oceanography Centre Southampton, University of Southampton, Southampton, UK, ³School of Earth Sciences, University of Bristol, Bristol, UK, ⁴Department of Earth Science and Engineering, Imperial College London, London, UK, ⁵Dipartimento di Scienze della Terra, Università di Pisa, Pisa, Italy, ⁶Department of Geography, University of Cambridge, Cambridge, UK, ⁷IPGP, Paris, France

Abstract Nabro volcano, situated to the east of the Afar Rift Zone, erupted on 12 June 2011. Eruptions at such off-rift volcanoes are infrequent, and consequently, the plumbing systems are poorly understood. We present posteruption Synthetic Aperture Radar (SAR) images from the TerraSAR-X satellite and posteruption continuous seismic activity from a local seismic array. Interferometric analysis of SAR data, reveals a circular, 12 km wide, signal subsiding at ~ 200 mm/yr. We inverted for the best fit Mogi source finding a $4 \pm 1 \times 10^7$ m³/yr volume decrease at 7 ± 1 km depth. Between 31 August and 7 October 2011, we located 658 and relocated 456 earthquakes with local magnitudes between -0.4 and 4.5 . Seismicity beneath the SE edge of Nabro at 11 km depth is likely associated with high strain rates from deep magma flow into the modeled reservoir. This suggests that magma is supplied through a narrow conduit and then stored at ~ 7 km depth. We interpret seismicity at 4–6 km depth as brittle fracturing above the inferred magma reservoir. Focal mechanisms delineate a thrust fault striking NE-SW and dipping 45° to the SE across the caldera floor. We propose that the crustal response is to slip on this fault which crosscuts the caldera rather than to deform on ring faults. The NE-SW fault plane is not associated with measurable surface deformation, indicating that it does not contribute much to the caldera deformation. We show that subsidence of the caldera is controlled by magma chamber processes rather than fault slip.

1. Introduction

During continental rifting the majority of active volcanism typically becomes focused in a central rift axis [Ebinger and Casey, 2001]. In the Afar region of Ethiopia, this is expressed as laterally stepping en echelon volcanic ranges that accommodate most of the extension [Hayward and Ebinger, 1996]. However, volcanic structures are also commonly found offset from the axis of spreading [Ebinger, 1989; Kiselev, 1987; Abebe et al., 1998; Sturkell et al., 2003; Bosworth et al., 2005]. Termed “off-axis” or “off-rift” volcanoes, their magma supply and their role in accommodating extension remains unclear [e.g., Maccaferri et al., 2014]. Furthermore, eruptions of off-rift volcanoes are infrequent, limiting opportunities to observe them when active. The eruption of Nabro volcano on 12 June 2011 was only the second eruption of an off-rift volcano associated with the Afar Rift Zone (ARZ) in modern times (since Dubbi volcano in 1861 [Wiert and Oppenheimer, 2000]). It was also the volcano’s first in the historical period [Wiert and Oppenheimer, 2005]. Here we analyze posteruption seismicity and Interferometric Synthetic Aperture Radar (InSAR)-derived surface deformation to understand the subsurface magmatic system of this hazardous, off-rift volcano.

Nabro volcano is located on the central part of the Danakil microplate on the southern margin of the Danakil Alps [Berhe, 1990] in NE Afar (Figure 1). It is the largest volcano in the ~ 110 km long Nabro Volcanic Range (NVR), which trends NNE-SSW and extends from Bara’ Ale volcano in Ethiopia to the Kod Ali formation in the Red Sea [Wiert and Oppenheimer, 2005]. A subsection of the NVR is the Bidu Volcanic Complex (BVC) composed of the Nabro and Mallahle calderas. Nabro comprises a horseshoe-shaped caldera reaching 8 km in diameter, open to the SW and facing the smaller 6 km diameter caldera of Mallahle volcano [Wiert and Oppenheimer, 2005]. The summit of Nabro is 2248 m above sea level (asl), making the BVC one of the largest massifs in the Afar region.

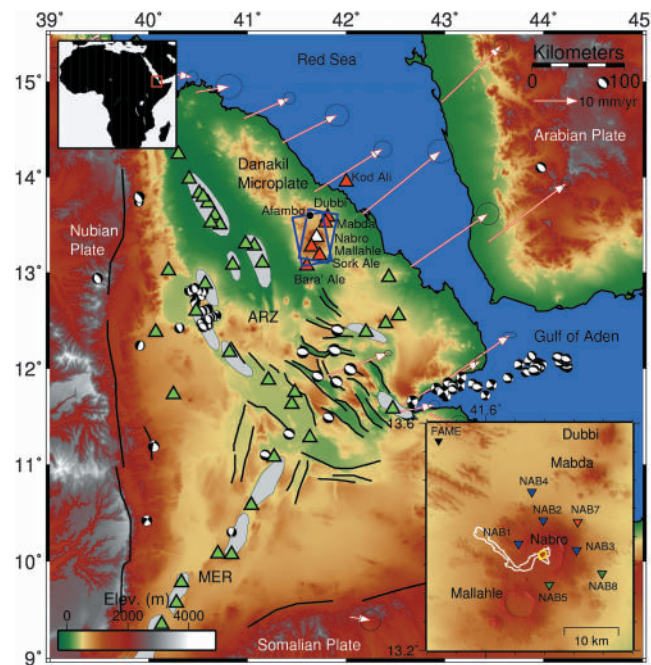


Figure 1. Topographic map (90 m Shuttle Radar Topography Mission) of the Afar Rift Zone (ARZ). Black lines are regional faults, and grey zones indicate volcanic segments. Fault plane solutions determined by the Global CMT project are displayed for earthquakes that occurred between 1979 and 11 June 2011; note the lack of events beneath the Nabro Volcanic Range (NVR). Green triangles indicate regional Holocene volcanoes recorded in the Smithsonian Catalogue “Volcanoes of the World” database, the red triangles constitute the NVR, with Nabro volcano highlighted in white. The white arrows represent measured horizontal GPS displacement relative to the Nubian plate [McClusky et al., 2010]. Blue boxes outline the footprint of TerraSAR-X Tracks 046 and 130. The black dot marks the village of Afambo. (bottom right inset) ASTER G-DEM topographic map of Nabro volcano. Inverted triangles show the configuration of seismic stations used for the analysis. Green: 40 TD Güralp seismic stations. Blue: 6 TD Güralp seismic stations. Red: 6 TD Güralp seismic station used for focal mechanism analysis only. Black: 3ESP seismic station, part of a regional array. White outline: 2011 eruption lava flow. Yellow: 2011 eruption vent region.

Between 23 February and 11 June 2011, nine earthquakes with local magnitudes ranging from 2.6 to 4.8 occurred in the BVC region [Goitom et al., 2014]. These were the first signs of forthcoming volcanic activity at Nabro in modern times. The eruption began between 20:30 and 20:45 UTC on 12 June 2011 from a circular vent region, centered on 41.7°E, 13.4°N and lasted approximately 2 weeks. Explosive phases of the eruption generated ash clouds which reached initial heights of 15–17 km [Clarisse et al., 2014] and disrupted aviation [Bojanowski, 2011]. In addition, an estimated 4.3 Tg of SO₂ were emitted to the atmosphere during the eruption [Theys et al., 2013]. This was the largest emission of SO₂ by an African volcano following the release of ~4.11 Tg SO₂ during the 1981–1982 eruption of Nyamulagira [Bluth and Carr, 2008]. The 2011 Nabro eruption was one of the most substantial volcanic SO₂ emissions since the 1991 eruption of Mount Pinatubo, which emitted ~20 Tg SO₂ to the atmosphere [Bluth et al., 1992]. A small crater just to the SW of the center of the caldera was the focus of the eruption. By 18 June 2011 this crater infilled with a tephra cone and a 2 km discontinuous alignment of small pits striking NW-SE opened up (Oppenheimer person.coms). A 17.5 km trachybasalt to

trachybasaltic andesite lava flow travelled for ~4 km SW from the vent region, before turning to the NW (Figure 1). In some places, such as near its terminus, the width of the lava flow is as much as 2 km. Flow margins reached 5–10 m in thickness, but the thickness of the interior of the flow could not be judged in the field and may be substantially higher in places. The extent of the eruption required the Southern Red Sea Administration (SRSA) to form response teams to coordinate the disaster [Solomon, 2012]. In total, seven people died, three were injured and 12,000 were displaced. The total cost of the eruption was estimated at 3 million USD [Solomon, 2012].

In this paper we present observations of the posteruption deformation obtained with high spatial resolution InSAR and microseismicity recorded between 31 August 2011 and 7 October 2011 using a local array. We invert the deformation field revealed by InSAR to model the subsurface change in magma source volume and associated geometry. In addition, we present hypocenters and magnitudes of the earthquakes recorded by the local seismic station network and use them in combination with the deformation data to interpret subsurface magma plumbing. We calculate fault plane solutions to quantify the style and orientation of fault slip in response to magma withdrawal and to study the evolution of the structure of the caldera after the eruption.

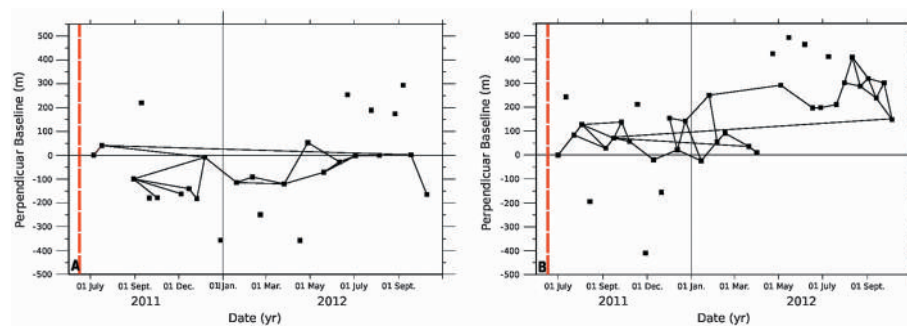


Figure 2. Perpendicular baseline versus time plot for (a) ascending track 130 and (b) descending track 046. Showing acquisitions (black squares) following the eruption. Solid lines represent interferograms where the unwrapping was above 90%. These interferograms are used for this InSAR analysis. Dates not connected were not used for the study. Red dashed line indicates the onset of the eruption.

2. InSAR Analysis

2.1. InSAR Data

The TerraSAR-X (TSX) satellite was tasked to acquire “StripMap” SAR images of the region following the eruption on both ascending and descending orbits. The TSX satellite uses an active X band SAR antenna with a wavelength of 31 mm, the incidence angle of the beam varies across the scene, between 25.1° to 30.5° and 31.7° to 34.8° for the ascending and descending tracks, respectively. Each fringe within an interferogram corresponds to a change in range of ~ 15 mm between the ground and the satellite. Each SAR scene is 30 km wide and 50 km long, large enough to cover the BVC and the surrounding area, with a minimum pixel size corresponding to 3 m on the ground. We used a data set of 25 images acquired between 1 July 2011 to 5 October 2012 on descending orbit 046 and complemented these with 19 images from ascending orbit 130 spanning the period between 6 July 2011 and 10 October 2012.

2.2. Method

The potential for spaceborne radar interferometry to monitor long-term deformation over active volcanoes was first demonstrated by *Massonnet et al.* [1995]. Subsequently, it has become an invaluable technique to study the ground displacements caused by magma movements due to the high spatial resolution and synoptic coverage of the data [e.g., *Amelung et al.*, 2000; *Lu et al.*, 2005; *Wright et al.*, 2006; *Biggs et al.*, 2011; *Hooper et al.*, 2012]. We created 34 interferograms from the descending data set and 21 interferograms from the ascending data set. The interferograms have a maximum perpendicular baseline of 200 m and temporal baseline between 11 and 390 days. We used a connected network of interferograms which had at least 90% of the image unwrapped (Figure 2). The interferograms were created using the JPL/Caltech ROI_PAC software [*Rosen et al.*, 2004], and we used the multiinterferogram method of *Biggs et al.* [2007] as implemented in π RATE [*Wang et al.*, 2012] to produce a rate map showing the average Line Of Sight (LOS) displacement rate of each pixel, as well as a time series of this displacement.

2.3. Results

In both ascending and descending data sets, we observe a nearly circular, ~ 12 km wide range increase, which is centered on the SW region of Nabro’s caldera (Figure 3). As the signal is a range increase in both data sets, the ground surface is moving away from the satellite. Therefore, the volcano is subsiding following the eruption. The caldera region within the descending rate map is incoherent, so we cannot measure the subsidence close to the vent region. In the descending track, the extent of the 17 km long lava flow emplaced by the eruption is also clearly distinguishable as an incoherent region originating from the caldera. There maybe a small localized loading effect within ~ 50 m of the lava flow. The ascending track is more coherent within the caldera; the maximum subsidence rate we measure is ~ 200 mm/yr. There is a small amount of LOS ground deformation at Mabda, Mallahle and Sork ‘Ale volcanoes observable from the ascending rate map (Figure 3); we interpret this as atmospheric noise caused by the topography of the volcanoes, as it is not visible in the descending data set. We have also plotted the subsidence over time (Figure 4) recorded at 1 pixel in the ascending data set. We find that the subsidence over the observation period is altogether quite linear but may have been faster immediately following the eruption. We go on to model the subsidence assuming a linear rate over time.

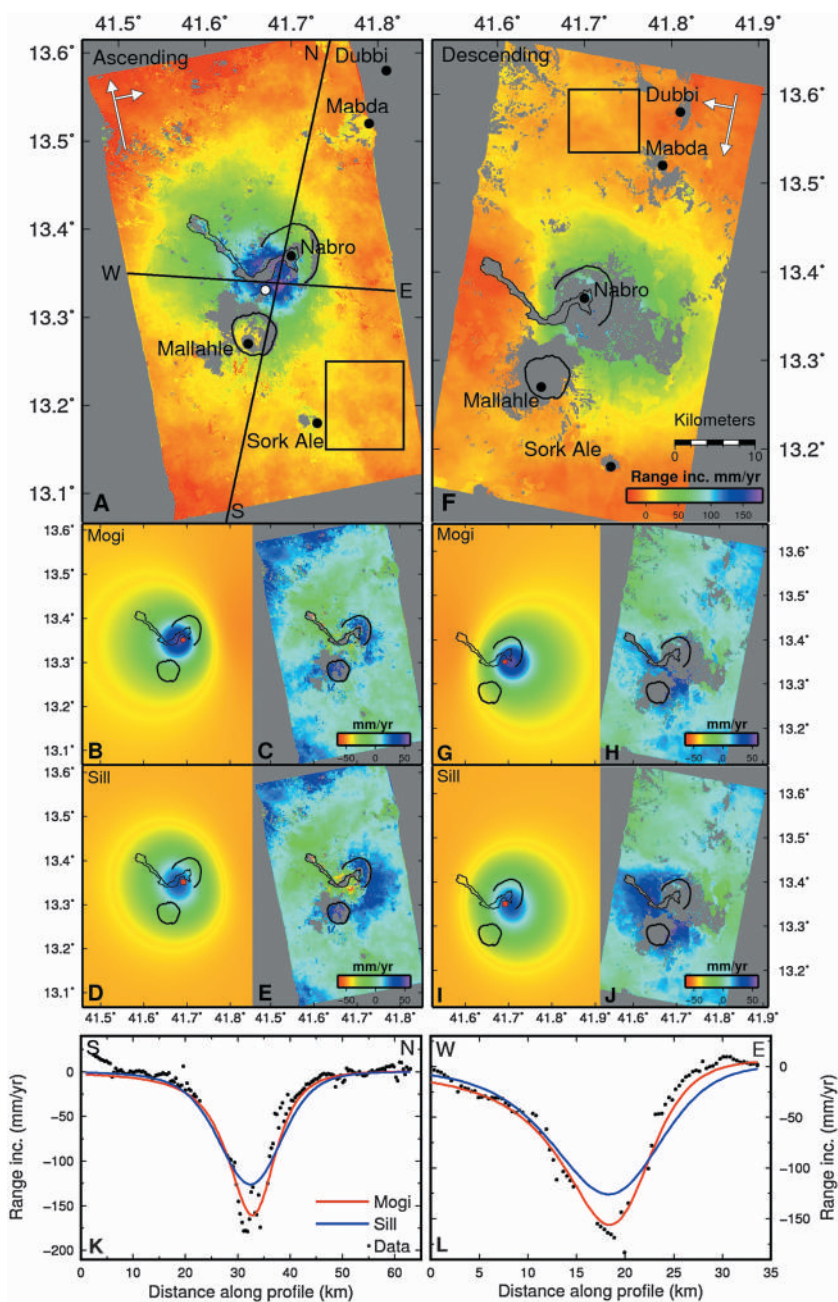


Figure 3. Best-fit model assuming Mogi and sill sources. (a) Observed ascending rate map of ground movement, white point: pixel used for time series. (b) Mogi model of deformation for ascending track. (c) Residual motion following Mogi model. (d) Sill model of deformation for ascending track. (e) Residual motion following sill model. (f) Observed descending rate map of ground movement. (g) Mogi model of deformation for descending track. (h) Residual ground motion. (i) Sill model of deformation for descending track. (j) Residual ground motion. (k) Profile of ground displacement along transect N-S on Figure 3a. (l) Profile of ground displacement along transect W-E on Figure 3a. The black squares in Figures 3a and 3f show the far-field regions used to calculate noise for the Monte Carlo analysis. The red points in Figures 3b, 3d, 3g, and 3i, mark the center of the model at depth. The interferograms span 462 days for both the ascending and descending tracks.

We jointly inverted the ascending and descending ground displacements using a Monte Carlo hybrid downhill simplex inversion technique [Clarke *et al.*, 1997; Wright *et al.*, 1999], which assumes a homogeneous, isotropic, Poisson-solid half space. The rate maps were averaged to 1 km pixels to reduce the inversion time. We first considered a deflating Mogi source in an elastic half space and solved for the depth, location, and volume change of the source (Figure 3). Uncertainties on these parameters were calculated using a Monte

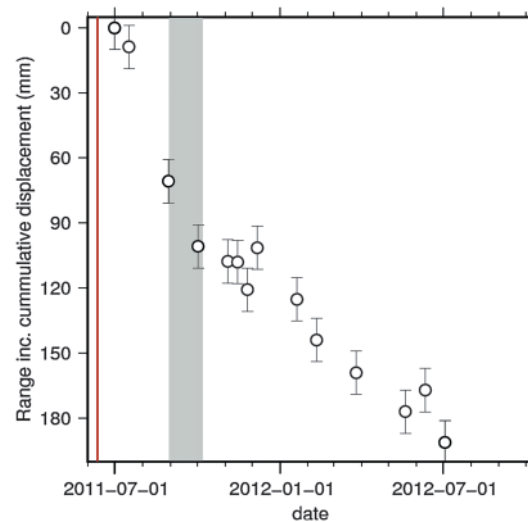


Figure 4. Time series of ground subsidence observed at the pixel marked by the white point on Figure 3a. The red line marks the onset of the eruption. Grey shading is the time period of the seismic data presented in this study.

of coherence in these areas due to the topography and ash cover or due to the model simplifications.

We also considered a sill geometry to model the subsidence. We used the same Monte Carlo hybrid downhill simplex inversion technique, and in the initial inversions, we solved for the location, depth, size (horizontal extent), and closing of a single-square Okada source [Okada, 1985]. However, the inversion collapsed to a small source with an unphysically large opening. Effectively, the only constraint on the size of the sill is that the horizontal extent of the sill is much less than the depth of the source. We therefore fix the horizontal extent of the sill to be 1 km in the subsequent inversions and only solve for the amount of closing. This is equivalent to solving for the contraction volume of a point source sill. We find that the best-fit sill is located at a depth of 11 ± 2 km; it has a contraction volume of $4 \pm 1.2 \times 10^7$ m³/yr, and on the surface, the center is located within 0.9 km of 13.35°N and within 0.6 km 41.69°E. As observed with the Mogi source, due to the nonuniqueness of InSAR modeling, there is still a trade-off between volume change and depth. The sill model underestimates the amount of subsidence at the center of Nabro's caldera, observable from the ascending track. Also, the sill solution does not account for much horizontal movement. This has resulted in higher residuals on the east and west flanks of Nabro in the ascending and descending tracks, respectively. The RMS misfit for the sill model is 13.9 mm/yr and 12.7 mm/yr for the ascending and descending tracks, respectively.

The Mogi model better describes the horizontal ground motions which are implied by the difference between the ascending and descending scenes, suggesting that the surface deformation is best approximated by a deflating point source. The model also captures the maximum surface displacement better than the sill source. Also, the RMS misfit is lower in both tracks and this is emphasized in the transects across the ascending data (Figures 3k and 3l). We have neglected the variation of topography for the inversion, and therefore, we have referenced all depths to 700 m asl, (the seismicity reference elevation). The interferometric analysis and modeling describes the ground displacement and gives an analytical solution to the magma chamber geometry. Using the seismic data we can improve the constraints on the depth of the magma chamber and observe the small scale brittle response to the eruption. These features will further delineate the magma plumbing system and may illuminate faults which accommodate the subsidence. We present the seismic data in the following section and provide a discussion of the integrated results.

3. Seismic Analysis

3.1. Seismic Data

In response to the eruption, we deployed a network of eight broadband Güralp seismic stations (five 6TD and three 40TD, provided by SEIS-UK [Brisbourne, 2012]) on the flanks of Nabro. The network was fully operational by 31 August 2011, 79 days after the eruption began. However, the GPS failed at NAB5 (6TD site)

Carlo simulation by adding correlated noise to the data set [Wright *et al.*, 2003], which was estimated from a background reference region located away from the deformation (Figure 3). We created 100 of such data sets, which were subsequently inverted. The range of the solutions gives the uncertainties of the parameters. We find the best-fitting Mogi source at 7 ± 1 km depth, which reduces in volume by $4 \pm 1 \times 10^7$ m³/yr, on the surface, the center is located within 0.6 km of 13.35°N and 41.69°E. From the Monte Carlo simulations we find a trade-off between the volume change and the depth of the source. The ground displacement modeled by the Mogi source has an RMS misfit of 13.2 mm/yr and 11 mm/yr for the ascending and descending tracks, respectively. The highest residuals in the ascending track are around the caldera rim, and highest in the descending track between Nabro and Mallahle calderas. This could be due to the loss

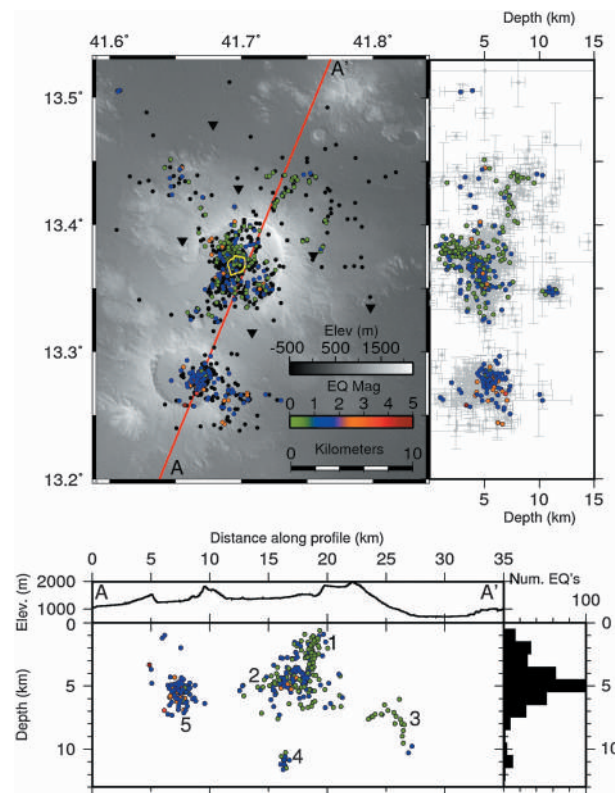


Figure 5. (top) Initial hypocenter locations determined using Hypo2000, for the 658 earthquakes detected during the period 31 August to 7 October 2011, shown as black dots (map view) and grey dots with error bars (N-S depth profile). The position of 456 relocated hypocenters calculated by HypoDD are shown as colored dots, dependent on their local magnitude. Seismic stations used to locate the events are indicated by black triangles. Yellow outline highlights the vent region. (bottom) Topographic profile and hypocenters along transect A-A', determined by HypoDD within 1 km either side of the transect. The depths are given referenced to 700 m asl, the lowest elevation seismometer. The histogram shows numbers of hypocenters at depth per 1 km bin. Numbers indicate clusters as described in text.

3.2. Methods

We manually picked arrival times of the *P* and *S* waves at every seismic station for each distinguishable earthquake using SAC software [Goldstein and Snoke, 2005]. We found that the traces did not need to be filtered before analysis due to the high data quality. As part of the process, we assigned a quality value of 0, 1, 2, and 3 to the measurement, based on an estimated *P* wave arrival time error of 0.05, 0.1, 0.015, and 0.2 s, respectively. For *S* waves, the 0 to 3 quality values were assigned to values of 0.1, 0.175, 0.25, and 0.3 s, for the estimated error in arrival time. These values were used as weights in the location inversion performed by the Hypo2000 algorithm [Klein, 2002] (Figure 5).

During the 38 day recording period we detected a total of 658 earthquakes on Nabro caldera and in the surrounding area. To locate earthquakes we used a 1-D velocity model with a linear increase in velocity with depth [Lahr, 1989]. This avoided clustering of earthquakes at velocity discontinuities, an artefact often observed in velocity models with homogeneous layers. Our velocity model was constrained using crustal scale reflection and refraction seismology across the Danakil blocks [Makris and Ginzburg, 1987]. The average location error using this technique is significant; ± 2 km horizontal, ± 4 km depth, and obscures detailed observations about the magmatic plumbing of the volcano [Jones and Stewart, 1997]. These errors result from a combination of factors including, station locations, available phases, accuracy of the arrival time measurement, and the validity of the velocity model [Waldhauser and Ellsworth, 2000].

and NAB6 (40TD site) was damaged due to flooding; data recorded at these stations were not used in this study; the resulting array configuration is depicted in Figure 1. All local array seismic stations have a natural frequency response of 30 s. In addition to the local network on Nabro, data recorded by FAME a Güralp 3ESP seismometer in the nearby village of Afambo (Figure 1), with a natural frequency response of 60 s, are included in the analysis. This seismometer is located approximately 35 km NW of the caldera and is part of an Eritrean regional array. The first data download was completed on 7 October 2011. These provide the 38 day data set investigated in this study, which covers the posteruption period (the eruption ended by late June–early July 2011). The data have a high signal-to-noise ratio due to a favorable recording environment; the noise levels are low as the equipment was located in small villages, sheltered from the wind and far from ocean noise. The use of a local network is crucial for detecting and accurately locating microseismicity, which can help reveal detailed magma migration pathways and the development of subsurface structures in response to an eruption [e.g., Aspinall et al., 1998; Roman et al., 2006; Ebinger et al., 2008; Keir et al., 2009; Lehto et al., 2010; Tarasewicz et al., 2012a, 2012b; Roman and Gardine, 2013]. Furthermore, the focal mechanisms can be tightly constrained due to the spatial distribution of the seismic stations.

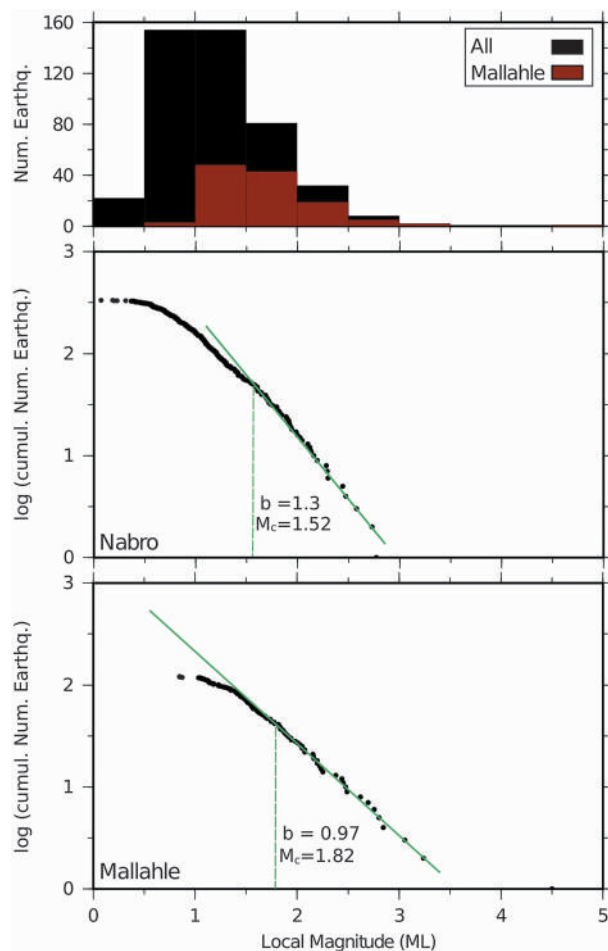


Figure 6. For all 658 events. (top) Distribution of the number of earthquakes at each magnitude. Black shows the distribution for all hypocenters, red shows the distribution for those which occurred on Mallahle caldera. (middle) Gutenberg-Richter distributions of the relocated earthquakes on Nabro. (bottom) Gutenberg-Richter distributions of the relocated earthquakes on Mallahle.

The Hypo2000 algorithm locates hypocenters assuming a 1-D subsurface. However, the velocity of a seismic wave beneath an active volcano will vary in three dimensions due to variations in rock composition and partially molten bodies. In addition, the subsurface velocity structure may also change through time as partial melt bodies evolve. We minimized the dependence of the hypocenter location on the velocity model by proceeding with a double differencing technique, HypoDD [Waldhauser and Ellsworth, 2000; Waldhauser, 2001], which we applied to the located events determined by Hypo2000, (Figure 5). We parameterized the relocation procedure in order to relocate the maximum number of events while minimizing the allowed separation between the initial hypocenters. In this manner, 456 of the initial 658 earthquakes were relocated.

Local magnitudes (M_L), as originally defined by Richter [1935], were computed using the maximum body wave amplitude of the horizontal component seismograms after they are convolved with the standard Wood-Anderson response [Anderson and Wood, 1925; Kanamori and Jennings, 1978]. The computation also considers the distance between the earthquake and stations in a distance correction term, which allows for decrease in amplitude with distance due to attenuation. We use the correction term derived for the Main Ethiopian Rift (MER) by Keir *et al.* [2006]. This correction is applicable to the high ground motion attenuation condi-

tions, caused by high heat flow due to the presence of partial melt beneath the rift valleys in the region [Gass, 1970; Keir *et al.*, 2011]. We use M_L estimates to calculate the seismic moment release using empirical relationships, e.g., Kanamori [1977], following the method of Keir *et al.* [2011].

We computed lower hemisphere focal mechanisms to constrain the orientation of crustal strains using FOCMEC [Snoke, 2003]. The program uses the station location, take off angles, and P and S_H wave polarities to perform a grid search for the best-fit double-couple solution [Snoke, 2003; Ebinger *et al.*, 2008]. Using an incremental step of 10° , all fault plane solutions have an error of $\leq \pm 20^\circ$ in strike and dip of the nodal planes. We were able to estimate 46 robust fault plane solutions beneath Nabro's caldera. We could not determine solutions for events away from the caldera due to the configuration of seismic stations. Data from the seismic station with a failed GPS system (NAB7) were included in the data set as the arrival time of the wave was not relevant for this analysis, but the position of the station was useful for determining the strike of the nodal planes.

3.3. Results
3.3.1. Spatial Variations

All of the events recorded can be defined as volcano-tectonic (VT) earthquakes as they have clear P and S wave arrivals, with an average peak frequency of 7 Hz [Lahr *et al.*, 1994]. VT earthquakes are commonly recorded at preeruption, coeruption, and posteruption and can indicate changes in the magmatic plumbing

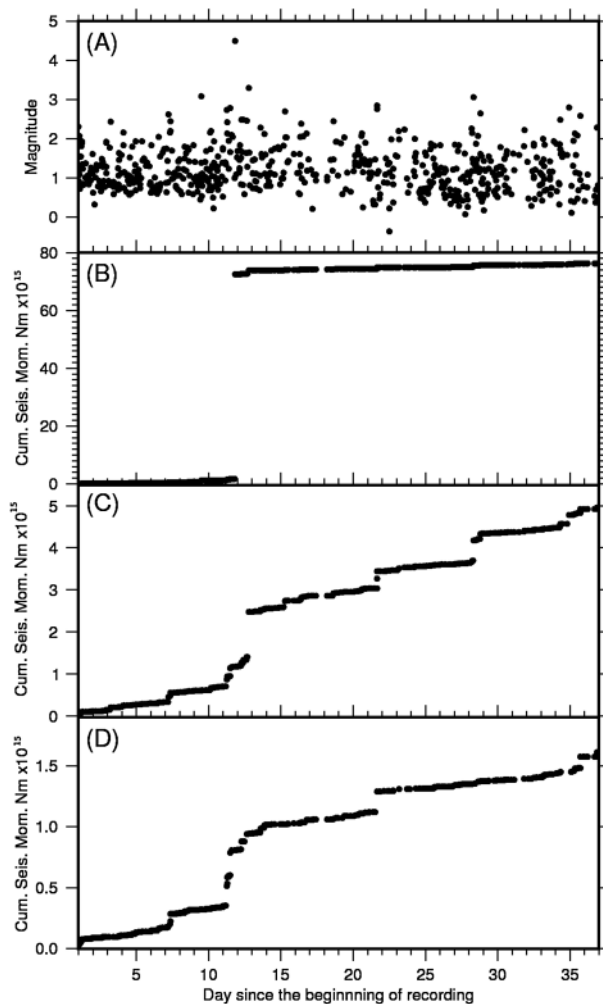


Figure 7. (a) Magnitude of 650 Hypo2000 located earthquakes over the 38 day recording period. (b) Cumulative seismic moment release of all earthquakes over the recording period. (c) Cumulative seismic moment release with the largest event removed. (d) Cumulative seismic moment for earthquakes under Nabro only.

system and emplacement of new intrusions [Hill, 1977; Umakoshi et al., 2001; Roman and Cashman, 2006; Roman et al., 2006]. Event locations after relocating with HypoDD are overlain on the Hypo2000 results (Figure 5). The relative error of the relocated earthquakes is ± 40 m in depth and ± 16 m in the horizontal coordinate. The depths are referenced to 700 m asl, the lowest elevation seismometer. Five clusters are visible in the spatial distribution of the earthquakes (Figure 5): (1) Directly beneath the vent, there is an elongate, subvertical cluster extending between 1 and 4 km depth. (2) The cluster is located beneath the central and southern part of the caldera, it is subhorizontal with the seismicity deepening to the SW, the cluster is ~ 5 km long and between 4 and 5 km deep. (3) Beneath the NE flank of Nabro, there is a NE striking cluster which deepens to the north, it is 6–11 km deep. (4) Beneath the SE caldera wall, 16 earthquakes are between 10 and 12 km deep. (5) A cluster lies directly beneath Mallahle, the hypocenters form a spherical cluster ranging between 4 km and 7 km deep. There is a noticeable aseismic zone between Nabro and Mallahle calderas. We will use these clusters to interpret fault slip induced by magma movement, highlighting potential magma pathways, as well as slip on larger scale preexisting faults induced by volume changes in magma reservoirs.

3.3.2. Magnitudes

We determined local magnitudes (M_L) to range between -0.37 and 4.5 , for all 658 earthquakes located using Hypo2000. The magnitudes of the relocated earthquakes are shown in Figure 5. The majority of earthquakes beneath Mallahle have a magnitude between 1 and 2, (Figure 6). Most of the events with a magnitude between 0 and 1 are located beneath Nabro, but this can reflect bias caused by the station distribution. In order to see how magnitudes are distributed and how they establish cutoff magnitudes, we used the frequency-magnitude distribution (FMD) [Gutenberg and Richter, 1944]:

$$\log N = a - bM_c, \tag{1}$$

where N is the cumulative number of earthquakes with a magnitude equal to or greater than M , a is a constant describing the rate of seismic activity in the study area, and b is the gradient of the FMD plot. M_c , also known as the “cutoff” magnitude, is the smallest magnitude of earthquake to which the catalog is complete; this is determined by the network sensitivity. As equation (1) uses only the maximum observed magnitude, the resulting b value tends to be too low [Bender, 1983]. Therefore, as our data only spans a short period, we use the maximum likelihood formula (2) as derived by Utsu [1965] to calculate the b value,

$$b = \frac{\log_{10} e}{M_a - M_c}, \tag{2}$$

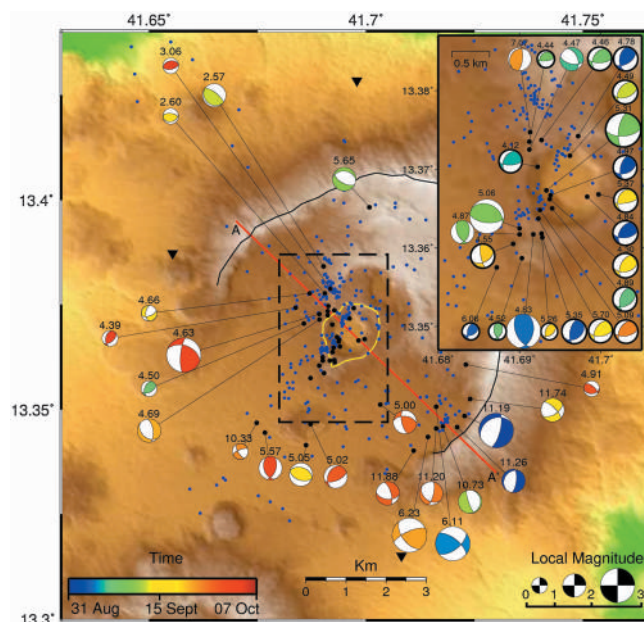


Figure 8. Lower hemisphere fault plane solutions for 46 earthquakes on Nabro; the location of the corresponding hypocenter is shown as a black dot. The size of the fault plane solution is scaled to the local magnitude of the event, and the depth at which it occurred is reported (in km) above the focal mechanism. All other earthquakes in the region are depicted with a blue dot. The color of the compressional quadrant of the solution is related to the time of the event. The 2011 eruption vent region is outlined in yellow, and the caldera rim is outlined in black. (inset) Zoom of the vent region with focal mechanisms. Eighteen thrust mechanisms are outlined in bold.

release of seismic energy can be attributed to an event with a magnitude > 4 . When this event is removed from the analysis (Figure 7c), it can be seen that the seismic moment release increases by between 0.2 and 0.4×10^{15} N m steps every 6–10 days with a linearly increasing moment release between each step. These linear increases with discrete steps are observed on both Nabro and Mallahle calderas. Figure 7d shows the seismic energy release from the events on Nabro only, these show the same trend as that observed in Figure 7c. There appears to be no consistent temporal pattern in the spatial distribution of events.

3.3.4. Focal Mechanisms

We computed 46 focal mechanisms beneath Nabro's caldera of which six were normal, 33 were thrust, and four were largely strike-slip motions (Figure 8). A prominent feature is a series of 18 thrust mechanisms with nodal planes striking NE-SW located in the center of the caldera, under the vent, which occur throughout the recording period at a depth between 4 and 5 km (Figure 8 (highlighted in bold), and Figure 9). In this region, there are three thrust mechanisms with differently orientated nodal planes; one striking northward and two with nodal planes striking ESE-WNW. Also in the center of the caldera, only one solution indicates normal faulting, the nodal planes strike SE-NW. Away from the center of the caldera, only nine of the 46 focal mechanisms have a major normal faulting component, four of which are located within the deep seismic cluster 4 (Figure 5). Due to the seismic network configuration, the focal mechanism of events beneath Mallahle caldera could not be constrained.

3.3.5. Waveforms

In order to test whether different earthquakes located close to each other are generated by the same slip motion in the same fault, we use the criteria of waveform similarities of earthquake pairs. Earthquake waveform pairs that have a significant similarity, expressed by a correlation coefficient greater than 0.7, are produced by the same source mechanism [Pechmann and Kanamori, 1982] and located within a distance of a 1/4 wavelength of each other [Geller and Mueller, 1980]. We can also use the correlation coefficients to qualitatively highlight changes in the subsurface. We have chosen two pairs of waveforms to perform the cross correlation, whose hypocenters are located within 215 m of each other, which is a 1/4 wavelength

where M_a is the average magnitude and M_c is the cutoff magnitude. Previous works by Bridges and Gao [2006] and Sanchez et al. [2004] show how spatial variations in b values can provide constraints on the distribution of magma in the subsurface. Therefore, we find separate b values for the events on Nabro and those on Mallahle. We plot the FMD for Nabro and Mallahle events separately (Figure 6). The b value was determined for Nabro using values of $M_a = 1.86$ and $M_c = 1.52$ and for Mallahle using $M_a = 2.62$ and $M_c = 1.82$. For all detected seismicity on Nabro, $b = 1.3 \pm 0.08$ for the events beneath Mallahle, $b = 0.97 \pm 0.15$ (Figure 6). The difference in cutoff magnitude between the two calderas is due to the siting seismic stations solely on Nabro. The seismic energy release will be compared to the accumulation of the seismic moment as determined by InSAR.

3.3.3. Temporal Variations

The daily number of earthquakes (Figure 7a) varies between 4 and 33 during the 38 day recording period. Figure 7b shows the original 658 earthquakes, which contribute 76×10^{15} N m seismic energy release. The largest

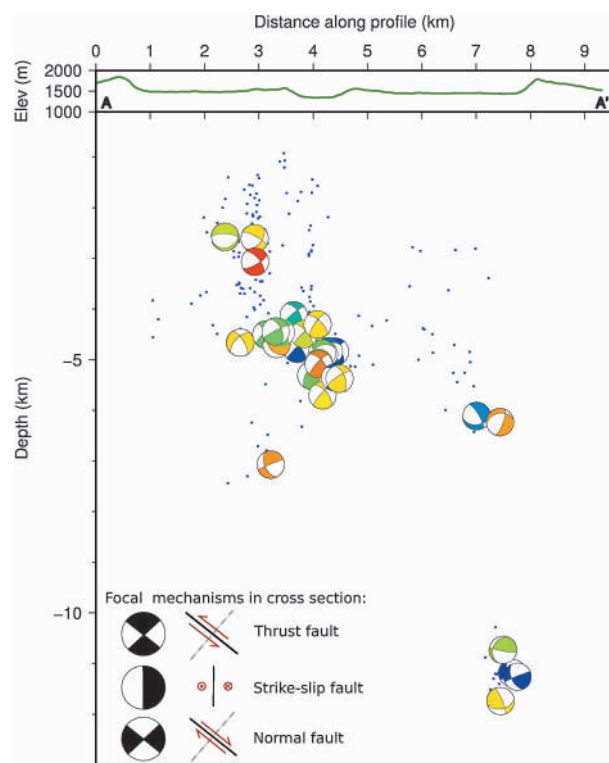


Figure 9. (top) Topography of Nabro along transect A-A'. (bottom) All focal mechanisms have been projected on to transect A-A' (Figure 6), then rotated to a side view, as viewed from south to north.

Nabro volcano. Using the high-resolution InSAR data in conjunction with seismicity, we are able to create a working model of the magmatic plumbing system and how it interacts with faults (Figure 11). We observe a circular subsidence signal which is offset to the SW of the caldera topography and the vent region, suggesting that the magma reservoir is not located directly beneath the eruption center. The subsidence signal suggests ongoing depressurization of the magma chamber following the eruption. The spatial pattern and sporadic nature of the hypocenters located at shallow depths (less than 6 km) under Nabro, are likely caused by the bending and episodic fracturing of brittle rocks within the volcanic edifice [Dzurisin *et al.*, 1991, 2002], in response to the depletion of the magma chamber. The temporal pattern of earthquake hypocenters has previously been used to show the migration of magma preceding and during eruptions [Tarasewicz *et al.*, 2012a]. However, beneath Nabro the seismicity recorded by the local array does not necessarily show this migration of magma to the surface, rather the constant reactivation of already developed faults, which slip during subsidence.

We find that the depth of the magma body, estimated by inverting the InSAR deformation field, is dependent on whether we chose a Mogi or sill source and the volume change imposed. The Mogi solution suggests a depth of 6.9 ± 1.1 km, whereas the sill solution yields a depth of 11 ± 2 km. Using the spatial distribution of the hypocenters, we suggest that the most applicable geometry of the source resembles the Mogi solution, as we interpret seismic cluster 2 (Figure 5) as the region of brittle failure immediately above the magma chamber, which fractures to accommodate the volume change. Therefore, the residual magma body is situated in the shadow zone immediately below this cluster. However, it is likely that the Mogi approximation is an oversimplification of the geometry of the magma source. A magma plumbing configuration of stacked sills was inferred from joint analysis of seismic, petrological, and geodetic data for Dabbahu volcano [Field *et al.*, 2012]. The magma reservoir under Nabro may also constitute numerous lenses and dykes of partial melt across a depth range of 6 to 10 km, which together approximate a single point source ground deformation signal. The deep cluster of seismicity (cluster 4, Figure 5) directly beneath this region may be related to small-scale fracturing around a constricted part of the plumbing system, potentially linking the shallow sources to a deeper reservoir, similar to an interpretation of lower-midcrustal seismicity at

distance for these waveforms and all have the same focal mechanism. The first waveform pair are separated by 22 days, whereas the second pair occurs almost simultaneously, just 10 min apart. These four seismic waveforms have a peak frequency of approximately 7 Hz and contain some higher-frequency noise, which we filtered by applying a bandpass filter with corner frequencies of 2 and 10 Hz (Figure 10). We determined a cross-correlation coefficient of 0.20 and 0.84 for the first and second pairs, respectively. This discrepancy indicates that despite a close source location and the same focal mechanism, the path effects between the source and the receiver changed significantly between the two earthquakes constituting the first pair. This leads us to suggest that the subsurface evolved over the recording period, due to the ongoing subsidence.

4. Discussion

4.1. Joint Interpretation of InSAR and Seismicity

In this study we have measured the crustal response to the 2011 eruption of

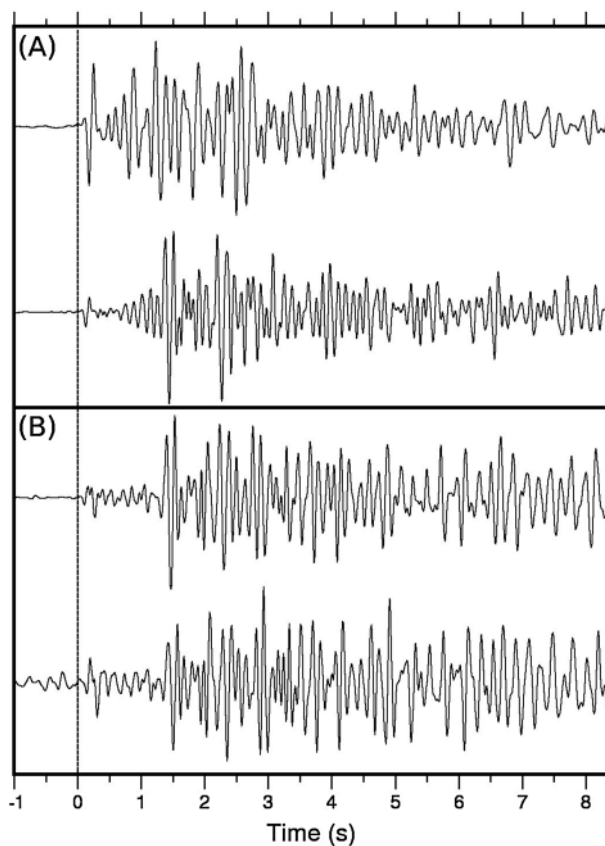


Figure 10. Examples of waveforms with a bandpass filter between 2 and 10 Hz applied. The hypocenters of the pairs are located within 215 m of each other. (a) Waveforms of earthquakes temporally separated by 22 days, with cross correlation of 0.20. (b) Waveforms of earthquakes temporally separated by 10 min, with cross correlation of 0.84.

Eyjafjallajökull volcano [Tarasewicz et al., 2012a]. However, this network of dikes and sills can not be fully constrained using the current data set. Furthermore, the accuracy of the interpretation of our results is based on analytical models which consider a homogeneous, isotropic, Poisson solid, half space with a horizontal free surface. Therefore, our interpretations are subject to the validity of such assumptions. *Masterlark* [2007] found that in the absence of additional geomechanical data regarding the mechanical properties of rock, an analytical model which makes the aforementioned assumptions is best, as the model is simple and fits the observations well. *Masterlark* [2007] also showed that topographic effects are insignificant if an appropriate reference elevation is used.

As the deformation at the vent is incoherent in the InSAR signal, we use the spatial distribution and focal mechanisms of the recorded earthquakes to delineate the small-scale brittle ground response. The vent region and potential conduit are highlighted by seismic cluster 1 (Figure 5). The InSAR subsidence signal is centered on Nabro caldera and does not extend laterally toward

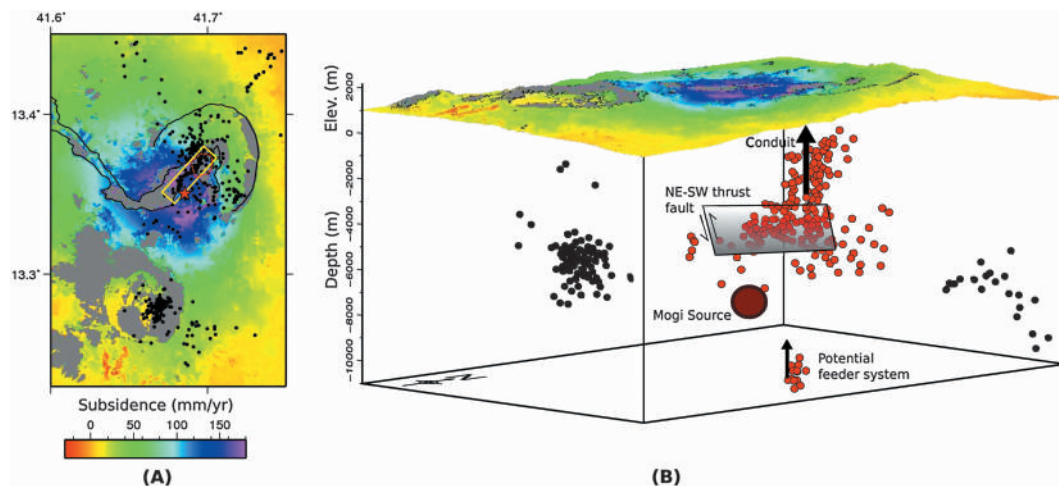


Figure 11. Working model of the magma plumbing system beneath Nabro. (a) Map view of the observed subsidence from the ascending InSAR data. Black outlines: caldera rim and lava flow. Red dashed line: vent region. Black dots: relocated hypocenters. Red star: Mogi model center. Yellow rectangle: NE-SW thrust fault outline at the surface. (b) Three-dimensional view of the proposed working model. Top plane: the observed subsidence from the ascending InSAR data draped on topography. Lower volume: hypocenter locations at depth. Red: earthquakes induced directly by the eruption. Black: regional earthquakes induced by changes to the stress field. The proposed Mogi source (dark red spot), conduit (large black arrow), thrust fault (grey plane), and potential magma supply system (small black arrow) are also highlighted.

Mallahle, which implies that there is no current subsurface magmatic connection between the two calderas. Therefore, the seismicity we observe is due to changes in the stress field resulting from the subsidence at Nabro and not caused by magma movement beneath Mallahle. However, a connection between the two calderas may have existed in the past. Also, the large magnitude ($M < 4$) VT earthquakes which occurred beneath Mallahle suggest that preexisting faults have been brought closer to failure, due to stress changes following the magma reservoir depressurization [Wauthier *et al.*, 2013a]. We interpret seismic cluster 3 to also be a result of the stress change, where the linear structure implies a fault which has been created or reactivated due to the new distribution of stress. We can not constrain the focal mechanisms of these events as they are located outside of the local seismic array. Also, as the earthquakes which highlight the fault have a maximum magnitude of 2 and are at a depth of ~ 8 km, even if we assume the fault to have a 90° dip and a thrust mechanism, the surface deformation associated with this inferred structure is less than 0.5 mm. Therefore, it is not observable using InSAR techniques despite good coherence in this area. As this fault plane is very speculative we have not included it in the working model (Figure 11).

4.2. Modes of Caldera Subsidence

The structure and evolution of calderas provide information on the behavior magma reservoir, and therefore, understanding their geometries is crucial in predicting future behavior [Cole *et al.*, 2005; Acocella, 2007]. We can compare the mode of subsidence implied by the focal mechanisms to models of caldera response. The seismic data reveal fault structures in the shallow subsurface (less than 6 km deep), the magnitudes of the earthquakes which delineate the fault have a maximum magnitude of 3. Earthquakes of this size at ~ 5 km depth cause less than 1 mm of deformation at the surface, which is not resolvable in the InSAR data. We also assess the temporal evolution of these faults through interpretation of the cross-correlated waveforms. In Figure 9, a thrust fault is observed to crosscut the caldera floor 1 km above the center of the magma source. Since the focal mechanisms define a 45° dip along one of the nodal planes (Figure 9), we infer that a fault plane strikes NE-SW, dipping 45° to the SE. We can compare this faulting to both numerical modeling performed by Holohan *et al.* [2011] and analog models [Lavallée *et al.*, 2004; Kennedy *et al.*, 2004; Roche *et al.*, 2000] to provide further insights into the mechanisms of subsidence. Holohan *et al.* [2011] used a two-dimensional finite element method to model the caldera subsidence in a half space with a range of geomechanical properties. If we qualitatively compare Figure 9 to Figure 5c in Holohan *et al.* [2011], we find similarities such as the dip and motion of the fault plane and its position relative to the magmatic body. Using the terminology of Holohan *et al.* [2011], our results could also be described as “reverse fault that separates two inward rotated roof blocks.” Quantitatively, the model we refer to would require the ratio between the thickness and diameter of the roof to be less than 0.33. Assuming that the seismicity under Nabro highlights the brittle failure of the roof, we find this ratio is between 0.69 and 0.88. As Nabro’s caldera is already well established, the fault plane we observe may have existed prior to the eruption and has been reactivated. This may explain the presence of the fault despite the higher ratio between the thickness and diameter of the roof. Furthermore, we observe a linear increase in the seismic energy release interrupted by discrete steps on a week time scale at Nabro, which is consistent with the findings of Ruch *et al.* [2012] that incremental collapses can occur on mature faults during caldera collapse. In the absence of appropriate measurements for bulk porosity, bulk density, and Young’s modulus for rocks at Nabro, the benefit of further quantitative application models such as that of Holohan *et al.* [2011] is limited.

Ring faults are a common feature of a caldera collapse [Marti *et al.*, 1994; Cole *et al.*, 2005]. However, the hypocenters we located are not concentrated on the caldera walls, implying that these structures may not have been activated during the eruption, which is not uncommon [Kennedy *et al.*, 2004]. In addition, the fault plane solutions of those found in the vicinity of the caldera walls are not tensional (Figure 9). The modeling by Holohan *et al.* [2011] shows an upward migration of faulting; therefore, the hypocenter locations are expected to migrate toward the surface over time. However, as no such pattern is observed within seismic cluster 1, the faults are assumed to have been formed before the local seismic array was deployed, and we only observe their sustained reactivation as the caldera relaxes. By comparing the waveforms of two pairs of earthquakes with adjacent hypocenters on the same fault plane but with each pair having a different temporal separation, we find a distinct decrease in correlation over time. This suggests that subsurface structures were evolving even during the recording period.

4.3. The b Values

The b values describe a region’s ability to accumulate stress, and the average global b value is approximately 1.0 [Richter, 1958]. However, b values can vary between regions as different geomechanical properties

influence the ability of rock to accumulate stress. Low b values indicate that a region is capable of accumulating significant stresses, which can result in large earthquakes. Areas with an increased thermal gradient [Warren and Latham, 1970] can be associated with a weak rheology, which cause small magnitude stress changes that tend to favor small-magnitude earthquakes. The lower b value for Mallahle implies that the earthquakes generated under Mallahle caldera are not dominated by magmatic processes and occur in rock with a stronger rheology. This is consistent with our conclusion that there is no subsurface magmatic link between Nabro and Mallahle calderas. The b value we calculated on Nabro is higher, likely due to a relatively weaker rheology, the presence of fluids and melt, the presence of highly fractured rock typical of heavily faulted calderas, and a higher geothermal gradient associated with the magma reservoir.

4.4. Off-Rift Volcanism

Off-rift volcanism is a common phenomenon that has also been observed in the Virunga Volcanic Province [Ebinger, 1989], in the Red Sea rift [Bosworth *et al.*, 2005], Iceland [Sturkell *et al.*, 2003], and the Baikal Rift [Kiselev, 1987]. Above the rift axis of the ARZ lie large volcanic provinces constructed from magma generated by decompression melting due to lithospheric thinning [Hammond *et al.*, 2013]. Pagli *et al.* [2012] suggest that an elevated magma supply in the rift axis of northern Afar results in shallow magma chamber depths, for example, the < 2.5 km depth chambers determined under Alu-Dalafilla and Dallo volcanoes [Pagli *et al.*, 2012; Nobile *et al.*, 2012]. Our results show that the magma plumbing system of the off-rift, flank volcanoes of the Danakil depression are fundamentally different from those in the rift axis and have deeper magma chamber depths. This is consistent with a lower spreading rate and thicker crust [Purdy *et al.*, 1992; Morgan and Chen, 1993; Chen and Morgan, 1996].

In rift settings the regional maximum compressive stress is vertical [Illies, 1981; Bosworth *et al.*, 1992]. On Nabro we expect the regional stress field to produce a vertical P axis and a NE striking T axis. However, our posteruption focal mechanisms show a horizontal NW striking P axis, revealing a local 90° shift from the expected regional orientation. Studies of VT earthquake swarms have documented a $\sim 90^\circ$ rotation of the P axis on volcanoes prior to and during eruptions, due to the propagation or inflation dikes [Roman and Cashman, 2006; Lehto *et al.*, 2010]. However, on Nabro we find that the 90° shift is present during the posteruption episode, while the volcano is subsiding, the NE-SW striking thrust fault is the geological expression of this stress field. We propose that this posteruption rotation observed on Nabro is due to the stress field induced by magma reservoir depressurization [Vargas-Bracamontes and Neuberg, 2012]. However, the fault geometry may also be influenced by the geomechanical structure of the caldera as well as changes to the magmatic plumbing system.

The NVR strikes oblique to the Red Sea rift, bisecting the Danakil microplate which is considered a relatively unrifted, coherent block [McClusky *et al.*, 2010; Hammond *et al.*, 2013]. Hammond *et al.* [2013] suggest that a thermal anomaly may be present, and some argue that increased melt production coincides with steep gradients in the lithosphere-asthenosphere boundary [Holtzman and Kendall, 2010; Rychert *et al.*, 2012]. However, these arguments do not explain the strike and extension of the NVR as a near continuous lineament from the ARZ to the Red Sea. Barberi *et al.* [1974] hypothesized that the NVR is a transverse structure, which developed through the rejuvenation of tectonically weak zones that preceded rift formation. The global CMT catalog shows that the majority of magnitude >4 earthquakes along the NVR have strike-slip and normal fault mechanisms. In addition to fault slip and style, the NEIC catalog of earthquakes shows that the NVR is also well delineated by a NE-SW striking alignment of earthquakes. The combination of fault slip style and earthquake locations on a regional scale show that the NVR has a transtensional motion, somewhat consistent with the previous interpretation in Barberi *et al.* [1974]. In addition, all of our focal mechanisms, which we use to constrain the NE-SW thrust fault crossing the caldera floor, have a strike-slip component. The orientation and strike slip could be due to a preexisting structural grain created by regional transverse motions, which was subsequently exploited during subsidence [Holohan *et al.*, 2008]. At Nyamulagira volcano a crosscutting caldera fault has also been observed during intereruptive periods, and it is considered to be a result of regional stresses [Wadge and Burt, 2011; Toombs and Wadge, 2012; Wauthier *et al.*, 2013b]. However, on Nabro we cannot differentiate between this cause of strike-slip motion and that produced by the caldera collapse itself. Horizontal motions caused by the interactions of numerous faults on the caldera floor can produce oblique slip faults [Holohan *et al.*, 2013]. The global CMT catalog of normal fault mechanisms and presence of volcanoes along the line suggest that the transform motion is accommodated by opening, partly accommodated by magma intrusion. Joint geological and geophysical data therefore show that the NVR may be analogous to a "leaky" transform fault, common on the magma-rich

ocean ridge system [Gregg *et al.*, 2007]. Our interpretation has the implication that the Danakil block may experience internal deformation and may be better approximated as two microplates either side of the NVR.

5. Conclusions

Our InSAR analysis of ascending and descending images, acquired after the eruption by the TSX satellite between 1 July 2011 and 10 October 2012, shows a concentric subsidence signal centered on Nabro's caldera with a maximum rate of 20 cm/year. The InSAR data can be modelled as a Mogi source at a depth of 6.9 ± 1.1 km. However, this may be an oversimplified model of magma reservoir geometry. We located 658, and relocated 456 earthquakes recorded over a 38 day period beginning on 31 August 2011. From the distribution of seismicity, we observe fracturing of brittle rock above the magma chamber. In conjunction with focal mechanisms, we delineate a major fault plane with a NE-SW strike which dips 45° to the SE, crosscutting the caldera floor. A deep cluster of seismicity suggests a link to a deeper magma source. The b value of the earthquakes beneath neighboring Mallahle volcano and the circular subsidence signal centered on Nabro, suggest that there is no subsurface magmatic link between Nabro and Mallahle calderas.

We observe a reverse fault which cuts through the center of the caldera floor and has the same NE-SW strike as the NVR. This mode of subsidence has been referred to as "snap style" [Holohan *et al.*, 2011]. In addition, this fault contains a strike-slip component, which is probably the result of a regional structural grain. The magma reservoir beneath Nabro is deep and this is only the second eruption of an off-rift volcano associated with the ARZ in modern times. We suggest that this is due to a low magma supply rate beneath Nabro in comparison to the volcanic centers on the rift axis. The majority of the subsidence is accounted for by the Mogi model. The seismicity represents minor deformation and is not required to account for the subsidence. Our results show that the posteruption subsidence of the caldera is controlled by the changes associated with the magma reservoir rather than significant slip on caldera ring faults, which were not activated during the post eruption phase that we have studied.

Acknowledgments

We would like to thank the Southern Red Sea Region Administration, Eritrea for support with the seismic deployments. The facilities of SEIS-UK are supported by the Natural Environment Research Council (NERC) under agreement R8/H10/64. Funding was provided by NERC grant NE/J012297/1 and NERC Fellowship NE/I020342/1 to J.O.S.H., and the NERC Centre for the Observation and Modelling of Earthquakes, volcanoes and Tectonics (COMET). Figures were produced using Generic Mapping Tools (GMT) [Wessel and Smith, 1998]. J.E.H. is funded through a NERC studentship at the University of Leeds. The seismic data is currently restricted, but will be uploaded to IRIS in October 2015 where it will be open access. TerraSAR-X data were provided under proposal GEO1206. The ascending and descending rate maps are available in .tif format as supporting information Figures S1 and S2. Raw RADAR data can be obtained by proposal from DLR using the website: <http://sss.terrasar-x.dlr.de/>.

References

- Abebe, T., F. Mazzarini, F. Innocenti, and P. Manetti (1998), The Yerer-Tullu wellel volcanotectonic lineament: A transtensional structure in central Ethiopia and the associated magmatic activity, *J. Afr. Earth Sci.*, *26*(1), 135–150.
- Acocella, V. (2007), Understanding caldera structure and development: An overview of analogue models compared to natural calderas, *Earth Sci. Rev.*, *85*(3), 125–160.
- Amelung, F., C. Oppenheimer, P. Segall, and H. Zebker (2000), Ground deformation near Gada 'Ale volcano, Afar, observed by radar interferometry, *Geophys. Res. Lett.*, *27*(19), 3093–3096.
- Anderson, J., and H. Wood (1925), Description and theory of the torsion seismometer, *Bull. Seismol. Soc. Am.*, *15*(1), 1–72.
- Aspinall, W., A. Miller, L. Lynch, J. Latchman, R. Stewart, R. White, and J. Power (1998), Soufrière Hills eruption, Montserrat, 1995–1997: Volcanic earthquake locations and fault plane solutions, *Geophys. Res. Lett.*, *25*(18), 3397–3400.
- Barberi, F., E. Bonatti, G. Marinelli, and J. Varet (1974), Transverse tectonics during the split of a continent: Data from the Afar rift, *Tectonophysics*, *23*(1), 17–29.
- Bender, B. (1983), Maximum likelihood estimation of b -values for magnitude grouped data, *Bull. Seismol. Soc. Am.*, *73*(3), 831–851.
- Berhe, S. M. (1990), Ophiolites in Northeast and East Africa: Implications for Proterozoic crustal growth, *J. Geol. Soc.*, *147*(1), 41–57.
- Biggs, J., T. Wright, Z. Lu, and B. Parsons (2007), Multi-interferogram method for measuring interseismic deformation: Denali fault, Alaska, *Geophys. J. Int.*, *170*(3), 1165–1179.
- Biggs, J., I. Bastow, D. Keir, and E. Lewi (2011), Pulses of deformation reveal frequently recurring shallow magmatic activity beneath the Main Ethiopian Rift, *Geochem. Geophys. Geosyst.*, *12*, Q0AB10, doi:10.1029/2011GC003662.
- Bluth, G., and S. Carn (2008), Exceptional sulfur degassing from Nyamuragira volcano, 1979–2005, *Int. J. Remote Sens.*, *29*(22), 6667–6685.
- Bluth, G. J., S. D. Doiron, C. C. Schmetzler, A. J. Krueger, and L. S. Walter (1992), Global tracking of the SO₂ clouds from the June, 1991 Mount Pinatubo eruptions, *Geophys. Res. Lett.*, *19*(2), 151–154.
- Bojanowski, A. (2011), Volcano mix-up, *Nat. Geosci.*, *4*(8), 495–495.
- Bosworth, W., M. Strecker, and P. Blisniuk (1992), Integration of east African paleostress and present-day stress data: Implications for continental stress field dynamics, *J. Geophys. Res.*, *97*(B8), 11,851–11,865.
- Bosworth, W., P. Huchon, and K. McClay (2005), The Red Sea and Gulf of Aden basins, *J. Afr. Earth. Sci.*, *43*(1), 334–378.
- Bridges, D. L., and S. S. Gao (2006), Spatial variation of seismic b -values beneath Makushin Volcano, Unalaska Island, Alaska, *Earth Planet. Sci. Lett.*, *245*(1), 408–415.
- Brisbourne, A. (2012), How to store and share geophysical data, *Astron. Geophys.*, *53*(4), 19–20.
- Chen, Y. J., and J. P. Morgan (1996), The effects of spreading rate, the magma budget, and the geometry of magma emplacement on the axial heat flux at mid-ocean ridges, *J. Geophys. Res.*, *101*(B5), 11,475–11,482.
- Clarisse, L., P.-F. Coheur, N. Theys, D. Hurtmans, and C. Clerbaux (2014), The 2011 Nabro eruption, a SO₂ plume height analysis using IASI measurements, *Atmos. Chem. Phys.*, *14*(6), 3095–3111.
- Clarke, P., D. Paradissis, P. Briole, P. England, B. Parsons, H. Billiris, G. Veis, and J.-C. Ruegg (1997), Geodetic investigation of the 13 May 1995 Kozani-Grevena (Greece) earthquake, *Geophys. Res. Lett.*, *24*(6), 707–710.
- Cole, J., D. Milner, and K. Spinks (2005), Calderas and caldera structures: A review, *Earth Sci. Rev.*, *69*(1), 1–26.
- Dzurisin, D., J. M. Donnelly-Nolan, J. R. Evans, and S. R. Walter (1991), Crustal subsidence, seismicity, and structure near Medicine Lake volcano, California, *J. Geophys. Res.*, *96*(B10), 16,319–16,333.

- Dzurisin, D., M. P. Poland, and R. Bürgmann (2002), Steady subsidence of Medicine Lake volcano, northern California, revealed by repeated leveling surveys, *J. Geophys. Res.*, *107*(B12), 2372, doi:10.1029/2001JB000893.
- Ebinger, C. (1989), Tectonic development of the western branch of the East African rift system, *Geol. Soc. Am. Bull.*, *101*(7), 885–903.
- Ebinger, C., and M. Casey (2001), Continental breakup in magmatic provinces: An Ethiopian example, *Geology*, *29*(6), 527–530.
- Ebinger, C., D. Keir, A. Ayele, E. Calais, T. Wright, M. Belachew, J. Hammond, E. Campbell, and W. Buck (2008), Capturing magma intrusion and faulting processes during continental rupture: Seismicity of the Dabbahu (Afar) rift, *Geophys. J. Int.*, *174*(3), 1138–1152.
- Field, L., J. Blundy, R. Brooker, T. Wright, and G. Yirgu (2012), Magma storage conditions beneath Dabbahu Volcano (Ethiopia) constrained by petrology, seismicity and satellite geodesy, *Bull. Volcanol.*, *74*(5), 981–1004.
- Gass, I. (1970), The evolution of volcanism in the junction area of the Red Sea, Gulf of Aden and Ethiopian rifts, *Philos. Trans. R. Soc. London, Ser. A*, *267*(1181), 369–381.
- Geller, R. J., and C. S. Mueller (1980), Four similar earthquakes in central California, *Geophys. Res. Lett.*, *7*(10), 821–824.
- Goitom, B., J. Hammond, M. Kendall, A. Nowacki, D. Keir, C. Oppenheimer, G. Ogubazghi, A. Ayele, S. Ibrahim, and E. Jacques (2014), Pre-, syn- and post eruptive seismicity of the 2011 eruption of Nabro volcano, Eritrea, *EGU General Assembly Conference Abstracts*, *16*, p. 6856, Vienna, Austria.
- Goldstein, P., and A. Snoke (2005), SAC availability for the IRIS community, *Incorporated Institutions for Seismology Data Management Center Electronic Newsletter*, *7*.
- Gregg, P. M., J. Lin, M. D. Behn, and L. G. Montési (2007), Spreading rate dependence of gravity anomalies along oceanic transform faults, *Nature*, *448*(7150), 183–187.
- Gutenberg, B., and C. F. Richter (1944), Frequency of earthquakes in California, *Bull. Seismol. Soc. Am.*, *34*(4), 185–188.
- Hammond, J., et al. (2013), Mantle upwelling and initiation of rift segmentation beneath the Afar Depression, *Geology*, *41*(6), 635–638.
- Hayward, N., and C. Ebinger (1996), Variations in the along-axis segmentation of the Afar Rift system, *Tectonics*, *15*(2), 244–257.
- Hill, D. P. (1977), A model for earthquake swarms, *J. Geophys. Res.*, *82*(8), 1347–1352.
- Holohan, E., M. Schöpfer, and J. Walsh (2011), Mechanical and geometric controls on the structural evolution of pit crater and caldera subsidence, *J. Geophys. Res.*, *116*, B07202, doi:10.1029/2010JB008032.
- Holohan, E. P., B. van Wyk de Vries, and V. R. Troll (2008), Analogue models of caldera collapse in strike-slip tectonic regimes, *Bull. Volcanol.*, *70*(7), 773–796.
- Holohan, E. P., T. R. Walter, M. P. Schöpfer, J. J. Walsh, B. van Wyk de Vries, and V. R. Troll (2013), Origins of oblique-slip faulting during caldera subsidence, *J. Geophys. Res. Solid Earth*, *118*, 1778–1794, doi:10.1002/jgrb.50057.
- Holtzman, B. K., and J.-M. Kendall (2010), Organized melt, seismic anisotropy, and plate boundary lubrication, *Geochem. Geophys. Geosyst.*, *11*, Q0AB06, doi:10.1029/2010GC003296.
- Hooper, A., F. Prata, and F. Sigmundsson (2012), Remote sensing of volcanic hazards and their precursors, *Proc. IEEE*, *100*(10), 2908–2930.
- Illies, J. H. (1981), Mechanism of graben formation, *Tectonophysics*, *73*(1), 249–266.
- Jones, R., and R. Stewart (1997), A method for determining significant structures in a cloud of earthquakes, *J. Geophys. Res.*, *102*(B4), 8245–8254.
- Kanamori, H. (1977), The energy release in great earthquakes, *J. Geophys. Res.*, *82*(20), 2981–2987.
- Kanamori, H., and P. C. Jennings (1978), Determination of local magnitude, ML, from strong-motion accelerograms, *Bull. Seismol. Soc. Am.*, *68*(2), 471–485.
- Keir, D., G. Stuart, A. Jackson, and A. Ayele (2006), Local earthquake magnitude scale and seismicity rate for the Ethiopian rift, *Bull. Seismol. Soc. Am.*, *96*(6), 2221–2230.
- Keir, D., I. D. Bastow, K. A. Whaler, E. Daly, D. G. Cornwell, and S. Hautot (2009), Lower crustal earthquakes near the Ethiopian rift induced by magmatic processes, *Geochem. Geophys. Geosyst.*, *10*, Q0AB02, doi:10.1029/2009GC002382.
- Keir, D., C. Pagli, I. D. Bastow, and A. Ayele (2011), The magma-assisted removal of Arabia in Afar: Evidence from dike injection in the Ethiopian rift captured using InSAR and seismicity, *Tectonics*, *30*, TC2008, doi:10.1029/2010TC002785.
- Kennedy, B., J. Stix, J. W. Vallance, Y. Lavallée, and M.-A. Longpré (2004), Controls on caldera structure: Results from analogue sandbox modeling, *Geol. Soc. Am. Bull.*, *116*(5–6), 515–524.
- Kiselev, A. (1987), Volcanism of the Baikal rift zone, *Tectonophysics*, *143*(1), 235–244.
- Klein, F. (2002), *User's Guide to HYPOINVERSE-2000: A Fortran Program to Solve for Earthquake Locations and Magnitudes*, U.S. Geol. Surv., Menlo Park, Calif.
- Lahr, J. (1989), *HYPOELLIPSE/VERSION 2.0*, A Computer Program for Determining Local Earthquake Hypocentral Parameters, Magnitude, and First Motion Pattern*, U.S. Geol. Surv., Menlo Park, Calif.
- Lahr, J., B. Chouet, C. Stephens, J. Power, and R. Page (1994), Earthquake classification, location, and error analysis in a volcanic environment: Implications for the magmatic system of the 1989–1990 eruptions at Redoubt Volcano, Alaska, *J. Volcanol. Geotherm. Res.*, *62*(1), 137–152.
- Lavallée, Y., J. Stix, B. Kennedy, M. Richer, and M.-A. Longpré (2004), Caldera subsidence in areas of variable topographic relief: Results from analogue modeling, *J. Volcanol. Geotherm. Res.*, *129*(1), 219–236.
- Lehto, H. L., D. C. Roman, and S. C. Moran (2010), Temporal changes in stress preceding the 2004–2008 eruption of Mount St. Helens, Washington, *J. Volcanol. Geotherm. Res.*, *198*(1), 129–142.
- Lu, Z., T. Masterlark, and D. Dzurisin (2005), Interferometric synthetic aperture radar study of Okmok Volcano, Alaska, 1992–2003: Magma supply dynamics and postemplacement lava flow deformation, *J. Geophys. Res.*, *110*, B02403, doi:10.1029/2004JB003148.
- Maccaferri, F., E. Rivalta, D. Keir, and V. Acocella (2014), Off-rift volcanism in rift zones determined by crustal unloading, *Nat. Geosci.*, *7*, 297–300.
- Makris, J., and A. Ginzburg (1987), The Afar depression: Transition between continental rifting and sea-floor spreading, *Tectonophysics*, *141*(1), 199–214.
- Marti, J., G. Ablay, L. T. Redshaw, and R. Sparks (1994), Experimental studies of collapse calderas, *J. Geol. Soc.*, *151*(6), 919–929.
- Massonnet, D., P. Briole, and A. Arnaud (1995), Deflation of Mount Etna monitored by spaceborne radar interferometry, *Nature*, *375*(6532), 567–570.
- Masterlark, T. (2007), Magma intrusion and deformation predictions: Sensitivities to the Mogi assumptions, *J. Geophys. Res.*, *112*, B06419, doi:10.1029/2006JB004860.
- McClusky, S., et al. (2010), Kinematics of the southern Red Sea–Afar Triple junction and implications for plate dynamics, *Geophys. Res. Lett.*, *37*, L05301, doi:10.1029/2009GL041127.
- Morgan, J. P., and Y. J. Chen (1993), Dependence of ridge-axis morphology on magma supply and spreading rate, *Nature*, *364*(6439), 706–708.

- Nobile, A., C. Pagli, D. Keir, T. J. Wright, A. Ayele, J. Ruch, and V. Acocella (2012), Dike-fault interaction during the 2004 Dallol intrusion at the northern edge of the Erta Ale ridge (Afar, Ethiopia), *Geophys. Res. Lett.*, *39*, L19305, doi:10.1029/2012GL053152.
- Okada, Y. (1985), Surface deformation due to shear and tensile faults in a half-space, *Bull. Seismol. Soc. Am.*, *75*(4), 1135–1154.
- Pagli, C., T. J. Wright, C. J. Ebinger, S.-H. Yun, J. R. Cann, T. Barrie, and A. Ayele (2012), Shallow axial magma chamber at the slow-spreading Erta Ale Ridge, *Nat. Geosci.*, *5*(4), 284–288.
- Pechmann, J. C., and H. Kanamori (1982), Waveforms and spectra of preshocks and aftershocks of the 1979 Imperial Valley, California, earthquake: Evidence for fault heterogeneity?, *J. Geophys. Res.*, *87*(B13), 10,579–10,597.
- Purdy, G., L. Kong, G. Christeson, and S. Solomon (1992), Relationship between spreading rate and the seismic structure of mid-ocean ridges, *Nature*, *355*, 815–817.
- Richter, C. (1935), An instrumental earthquake magnitude scale, *Bull. Seismol. Soc. Am.*, *25*(1), 1–32.
- Richter, C. F. (1958), *Elementary Seismology*, p. 578, W. H. Freeman and Co., San Francisco, Calif.
- Roche, O., T. Druitt, and O. Merle (2000), Experimental study of caldera formation, *J. Geophys. Res.*, *105*(B1), 395–416.
- Roman, D., J. Neuberg, and R. Luckett (2006), Assessing the likelihood of volcanic eruption through analysis of volcanotectonic earthquake fault-plane solutions, *Earth Planet. Sci. Lett.*, *248*(1), 244–252.
- Roman, D. C., and K. V. Cashman (2006), The origin of volcano-tectonic earthquake swarms, *Geology*, *34*(6), 457–460.
- Roman, D. C., and M. D. Gardine (2013), Seismological evidence for long-term and rapidly accelerating magma pressurization preceding the 2009 eruption of Redoubt volcano, Alaska, *Earth Planet. Sci. Lett.*, *371*, 226–234.
- Rosen, P. A., S. Hensley, G. Peltzer, and M. Simons (2004), Updated repeat orbit interferometry package released, *Eos Trans. AGU*, *85*(5), 47.
- Ruch, J., V. Acocella, N. Geshi, A. Nobile, and F. Corbi (2012), Kinematic analysis of vertical collapse on volcanoes using experimental models time series, *J. Geophys. Res.*, *117*, B07301, doi:10.1029/2012JB009229.
- Rychert, C. A., J. O. Hammond, N. Harmon, J. M. Kendall, D. Keir, C. Ebinger, I. D. Bastow, A. Ayele, M. Belachew, and G. Stuart (2012), Volcanism in the Afar Rift sustained by decompression melting with minimal plume influence, *Nat. Geosci.*, *5*(6), 406–409.
- Sanchez, J., S. McNutt, J. Power, and M. Wyss (2004), Spatial variations in the frequency-magnitude distribution of earthquakes at Mount Pinatubo volcano, *Bull. Seismol. Soc. Am.*, *94*(2), 430–438.
- Snoko, J. A. (2003), 85.12 FOCMEC: FOCal MEchanism determinations, *Int. Geophys.*, *81*, 1629–1630.
- Solomon, A. (2012), *Summary of Activities of the Southern Red Sea Administration During the Nabro Eruption*, Dep. of Infrastructure of the Southern Red Sea Admin., Assab, Eritrea.
- Sturkell, E., F. Sigmundsson, and P. Einarsson (2003), Recent unrest and magma movements at Eyjafjallajökull and Katla volcanoes, Iceland, *J. Geophys. Res.*, *108*(B8), 2369, doi:10.1029/2001JB000917.
- Tarasiewicz, J., B. Brandsdóttir, R. White, M. Hensch, and B. Thorbjarnardóttir (2012a), Using microearthquakes to track repeated magma intrusions beneath the Eyjafjallajökull stratovolcano, Iceland, *J. Geophys. Res.*, *117*, B00C06, doi:10.1029/2011JB008751.
- Tarasiewicz, J., R. S. White, A. W. Woods, B. Brandsdóttir, and M. T. Gudmundsson (2012b), Magma mobilization by downward-propagating decompression of the Eyjafjallajökull volcanic plumbing system, *Geophys. Res. Lett.*, *39*, L19309, doi:10.1029/2012GL053518.
- Theys, N., et al. (2013), Volcanic SO₂ fluxes derived from satellite data: A survey using OMI, GOME-2, IASI and MODIS, *Atmos. Chem. Phys.*, *13*(12), 5945–5968.
- Toombs, A., and G. Wadge (2012), Co-eruptive and inter-eruptive surface deformation measured by satellite radar interferometry at Nyamuragira volcano, DR Congo, 1996 to 2010, *J. Volcanol. Geotherm. Res.*, *245*, 98–122.
- Umakoshi, K., H. Shimizu, and N. Matsuwo (2001), Volcano-tectonic seismicity at Unzen volcano, Japan, 1985–1999, *J. Volcanol. Geotherm. Res.*, *112*(1), 117–131.
- Utsu, T. (1965), A method for determining the value of b in a formula $\log n = a - b m$ showing the magnitude-frequency relation for earthquakes, *Geophys. Bull. Hokkaido Univ.*, *13*, 99–103.
- Vargas-Bracamontes, D., and J. Neuberg (2012), Interaction between regional and magma-induced stresses and their impact on volcano-tectonic seismicity, *J. Volcanol. Geotherm. Res.*, *243*, 91–96.
- Wadge, G., and L. Burt (2011), Stress field control of eruption dynamics at a rift volcano: Nyamuragira, DR Congo, *J. Volcanol. Geotherm. Res.*, *207*(1), 1–15.
- Waldhauser, F. (2001), hypoDD—A program to compute double-difference hypocenter locations (hypoDD version 1.0-03/2001), *U.S. Geol. Surv. Open File Rep.*, *01*, 113.
- Waldhauser, F., and W. Ellsworth (2000), A double-difference earthquake location algorithm: Method and application to the northern Hayward fault, California, *Bull. Seismol. Soc. Am.*, *90*(6), 1353–1368.
- Wang, H., T. J. Wright, Y. Yu, H. Lin, L. Jiang, C. Li, and G. Qiu (2012), InSAR reveals coastal subsidence in the Pearl River Delta, China, *Geophys. J. Int.*, *191*(3), 1119–1128.
- Warren, N. W., and G. V. Latham (1970), An experimental study of thermally induced microfracturing and its relation to volcanic seismicity, *J. Geophys. Res.*, *75*(23), 4455–4464.
- Wauthier, C., D. C. Roman, and M. P. Poland (2013a), Moderate-magnitude earthquakes induced by magma reservoir inflation at Kilauea volcano, Hawaii, *Geophys. Res. Lett.*, *40*, 5366–5370, doi:10.1002/2013GL058082.
- Wauthier, C., V. Cayol, M. Poland, F. Kervyn, N. d'Oreye, A. Hooper, S. Samsonov, K. Tiampo, and B. Smets (2013b), Nyamuragira's magma plumbing system inferred from 15 years of InSAR, *Geol. Soc. London Spec. Publ.*, *380*(1), 39–65.
- Wessel, P., and W. H. Smith (1998), New, improved version of Generic Mapping Tools released, *Eos Trans. AGU*, *79*(47), 579.
- Wiat, P., and C. Oppenheimer (2000), Largest known historical eruption in Africa: Dubbi volcano, Eritrea, 1861, *Geology*, *28*(4), 291–294.
- Wiat, P., and C. Oppenheimer (2005), Large magnitude silicic volcanism in north Afar: The Nabro Volcanic Range and Ma'alalata Volcano, *Bull. Volcanol.*, *67*(2), 99–115.
- Wright, T., B. Parsons, J. Jackson, M. Haynes, E. Fielding, P. England, and P. Clarke (1999), Source parameters of the 1 October 1995 Dinar (Turkey) earthquake from SAR interferometry and seismic bodywave modelling, *Earth Planet. Sci. Lett.*, *172*(1), 23–37.
- Wright, T. J., Z. Lu, and C. Wicks (2003), Source model for the m_w 6.7, 23 October 2002, Nenana Mountain Earthquake (Alaska) from InSAR, *Geophys. Res. Lett.*, *30*(18), 1974, doi:10.1029/2003GL018014.
- Wright, T. J., C. Ebinger, J. Biggs, A. Ayele, G. Yirgu, D. Keir, and A. Stork (2006), Magma-maintained rift segmentation at continental rupture in the 2005 Afar dyking episode, *Nature*, *442*(7100), 291–294.